Progress In Electromagnetics Research C, Vol. 169, 185–196, 2026

(Received 12 March 2026, Accepted 19 April 2026, Scheduled 28 April 2026)

Quad-Mode CMA-Driven Circularly Polarized Metasurface MIMO Antenna

Yuhao Wei[1], Zhonggen Wang[1], Wenyan Nie[2,*], and Han Lin[1]

[1] *School of Electrical and Information Engineering, Anhui University of Science and Technology, Huainan 232001, China*
[2] *School of Mechanical and Electrical Engineering, Huainan Normal University, Huainan 232001, China*

ABSTRACT: This paper proposes a four-mode circularly polarized metasurface multiple-input multiple-output (MIMO) antenna based on characteristic mode analysis (CMA), which can be applied to Sub-6 GHz communications, unmanned aerial vehicle communications, wireless local area network, and other scenarios. Its core geometric novelty is a gradient-scaled 4×4 metasurface radiating layer: central units with corner truncation and 45° rotated rectangular stubs, and four corner units scaled down to 0.75 times the central size. This structure generates the 90° phase difference for CP radiation, synchronously exciting two orthogonal characteristic mode pairs to realize broadband CP radiation, and endows the metasurface with inherent self-decoupling capability. In addition, a 2×2 MIMO array is constructed by combining four monopole antenna elements, and the mutual coupling is suppressed by the metasurface itself, achieving a port isolation greater than 25 dB. Simulation and measurement results show that the impedance bandwidth is 41.93% (5.07–7.76 GHz), the axial ratio (AR) bandwidth is 17.5% (5.37–6.40 GHz), the peak gain is 6.77 dBi, the array envelope correlation coefficient is as low as 0.0002, and the diversity gain reaches 9.999 dB. The antenna achieves an excellent balance among broadband performance, high isolation, and structural simplicity, outperforming existing similar designs.

1. INTRODUCTION

Wireless communication technology is experiencing rapid development, which puts forward higher-dimensional requirements for antenna performance. In this context, circularly polarized (CP) antennas have become a key means to improve system reliability due to their inherent advantages, such as effective suppression of polarization mismatch, overcoming multipath fading, and adaptation to dynamic transmitting and receiving attitudes [1–3]. Their radiation characteristics provide an effective solution to the communication bottlenecks in high-speed mobile scenarios and complex electromagnetic environments. Therefore, CP antenna technology has shown indispensable application potential in satellite communication, radar detection, unmanned aerial vehicle (UAV) image transmission, and next-generation mobile communication systems [4].

To achieve these characteristics, researchers have applied various technologies and adopted new structures. Ref. [5] excited two orthogonal linearly polarized modes through coplanar waveguide feeding, achieving an AR bandwidth of 19.42%. Ref. [6] realized an AR bandwidth of 20.5% using a hybrid feeding system composed of a cross slot coupling and a circular microstrip line. In addition, researchers have proposed many methods to expand the AR bandwidth, such as multi-layer structures [7], multi-feeding structures [8], and air gap structures [9]. Although these schemes can achieve broadband characteristics, the complexity of the antenna structure increases significantly with the increase of antenna layers and feeding ports. In contrast, the simple-structured single-feed multi-mode excitation design remains a research focus due to its potential for bandwidth expansion.

The theory of CMA, proposed in the early 1960s [10], can effectively guide the excitation of multi-order characteristic current modes and provide support for the design of broadband CP antennas. In [11] and [12], the frequency interval of two characteristic modes was compressed, achieving AR bandwidths of 3% and 8.5%, respectively. In recent years, the research focus has shifted to exciting a greater number of high-order modes to fuse multiple resonance points, thereby greatly expanding the operating bandwidth. For example, Ref. [13] achieved an impedance bandwidth of 21.1% by exciting three-order linearly polarized modes; Ref. [14] significantly improved the AR bandwidth to 92.3% through four-order mode fusion. These advances fully indicate that the multi-mode excitation strategy based on CMA is an effective approach to break through the bandwidth limitation of traditional CP antennas.

In addition, MIMO antennas have demonstrated high efficiency due to their ability to effectively meet the demand for high data rate transmission and reduce signal fading, multipath effects, and interference. A dual CP four-port MIMO antenna proposed in [15] has an AR bandwidth of less than 20%. Ref. [16] reported a four-element MIMO antenna with a maximum impedance bandwidth of 91.5%, but the antenna is linearly polarized. Although Ref. [17] addressed the above problems, the additional feeding network and multi-layer structure design led to a significant increase in the volume and profile height of the antenna. The multi-layer large-size antenna element schemes proposed in [18] and [19] are not suitable for the design of compact broadband CP MIMO antenna arrays.

---

* Corresponding author: Wenyan Nie (wynie5240@163.com).

doi:10.2528/PIERC26031207

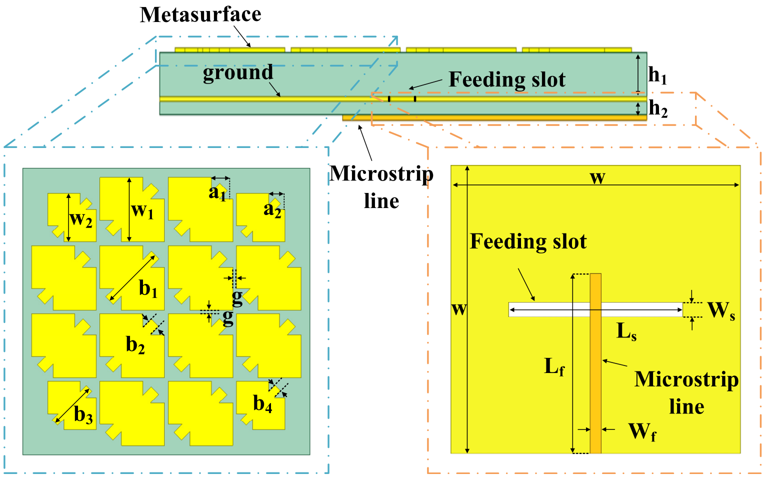

FIGURE 1. CP metasurface architecture. $w = 40\,\text{mm}$; $h_1 = 2\,\text{mm}$; $h_2 = 0.6\,\text{mm}$; $w_1 = 9\,\text{mm}$; $g = 0.5\,\text{mm}$; $a_1 = 3\,\text{mm}$; $b_1 = 9\,\text{mm}$; $b_2 = 1.5\,\text{mm}$; $L_s = 24\,\text{mm}$; $W_s = 2\,\text{mm}$; $L_f = 25\,\text{mm}$; $W_f = 1.5\,\text{mm}$; $w_2 = 6.75\,\text{mm}$; $a_2 = 2.25\,\text{mm}$; $b_3 = 6.75\,\text{mm}$; $b_4 = 1.125\,\text{mm}$.

Therefore, it remains a challenging research topic to synergistically achieve a wide impedance bandwidth, a wide AR bandwidth, and high port isolation in a limited space to fabricate a compact MIMO antenna system.

In summary, existing CP MIMO antennas still have certain contradictions in terms of broadband operation, high isolation, and structural simplicity. Traditional designs are difficult to balance wide impedance bandwidth, wide AR bandwidth, and high port isolation while maintaining a simple structure and easy integration. To address this issue, this paper proposes a four-mode CP metasurface MIMO antenna based on CMA. Guided by CMA, the patch shape is optimized, and corner truncation and a central rotated stub are adopted to achieve stable CP radiation. A microstrip-slot coupled feeding method is utilized to accurately excite orthogonal characteristic modes. Furthermore, a 2×2 MIMO array is constructed, and strong mutual coupling suppression is realized by virtue of the metasurface structure, achieving high isolation without additional decoupling structures. Simulation and measurement results verify the excellent performance of the proposed antenna in terms of bandwidth, gain, and high isolation, which can meet the application requirements of high-performance CP MIMO antennas in scenarios such as Sub-6 GHz mobile communications, UAV communications, and high-speed wireless local area networks.

2. ANTENNA DESIGN AND ANALYSIS

2.1. Antenna Configuration

Figure 1 shows the structural model and optimized dimensional parameters of the proposed CP metasurface antenna. The structure adopts three metal layers, which are, from top to bottom, a metasurface radiating patch layer, a metal ground plane layer with a rectangular coupling slot etched in the center, and a microstrip feeder layer. Two dielectric substrates are both made of FR-4 (relative permittivity $\varepsilon_r = 4.4$, loss tangent $\tan\delta = 0.025$) with thicknesses of h_1 and h_2, respectively, and the overall size is $40 \times 40 \times 2.6\,\text{mm}^3$.

The metasurface layer adopts a 4×4 structure, where the side length of the central unit is w_1, and the unit spacing is g. The structural feature of the central unit is that a square area with a side length of a_1 is cut off at both the upper right corner and the lower left corner, followed by a rectangular patch with a size of $b_1 \times b_2$ rotated by 45° added in the center. The units located at the four corners of the array are scaled down by 0.75 times from the central unit, with the scaled side length being w_2. Correspondingly, the side length of the cut-off rectangles at the upper right and lower left corners is adjusted to a_2, and the length and width of the rotated 45° rectangular patch added in the center are adjusted to b_3 and b_4, respectively. A rectangular coupling slot with a length of L_s and a width of W_s is etched in the center of the ground plane layer shown. The bottom layer is composed of a microstrip feeder with a length of L_f and a width of W_f. Microwave energy is coupled from the rectangular slot to the metasurface through the microstrip line.

2.2. Characteristic Mode Analysis

Based on the theory of CMA, the metasurface structure was simulated using the built-in CMA tool in Computer Simulation Technology (CST) 2022. As shown in Fig. 2(b), the characteristic angle (CA) difference between Mode 2 and Mode 4 near 5.8 GHz is approximately 90°. In addition, as illustrated in Fig. 2(c), around 5.8 GHz, the modal currents of Mode 2 and Mode 4 are concentrated in the central four patch regions, with polarization directions of $-45°$ and $-135°$, respectively, forming an orthogonal current pair. The two modes exhibit similar and excellent far-field radiation patterns on the broadside. Therefore, the set of orthogonal modes formed by Mode 2 and Mode 4 can meet the requirements for generating CP.

On the other hand, the CA difference between Mode 5 and Mode 9 near 6.5 GHz is approximately 90°; the modal currents of the four central patches in Mode 5 and Mode 9 are polarized at 45° and 135° respectively. Although the modal currents of the peripheral patches in Mode 9 are opposite to those of the central patch, their radiation patterns still have verticality. If

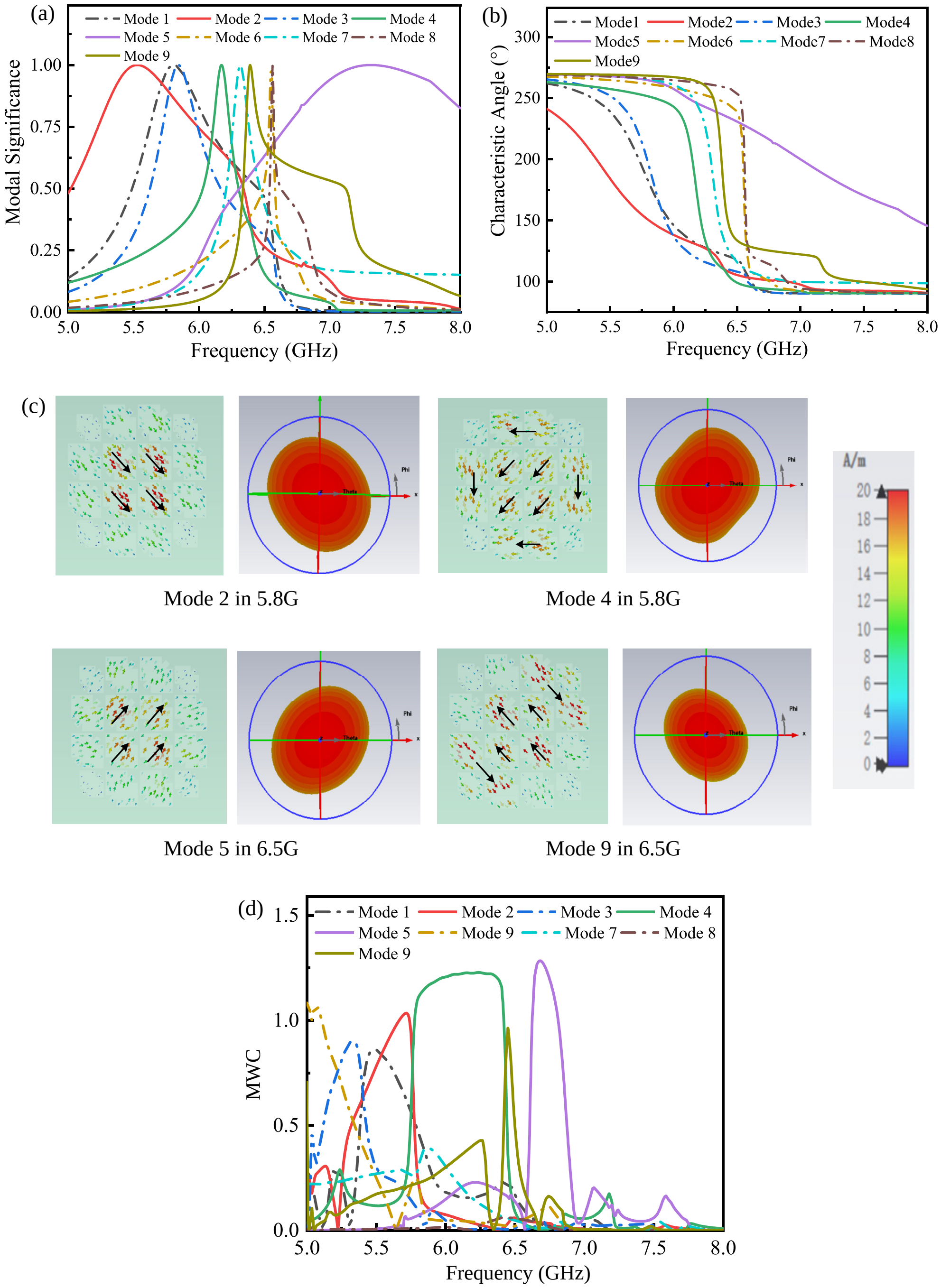

Mode 2 in 5.8G

Mode 4 in 5.8G

Mode 5 in 6.5G

Mode 9 in 6.5G

FIGURE 2. CMA results for the first nine characteristic modes. (a) MS. (b) CA. (c) Modal current distributions and radiation patterns for Mode 2 and Mode 4 at 5.8 GHz, and Mode 5 and Mode 9 at 6.5 GHz. (d) MWC.

a feeding position is set at the central patch, it can also meet the requirements for the generation of CP. By cooperatively exciting the above two sets of orthogonal modes (Mode 2/4 and Mode 5/9), a multi-mode superposition effect is achieved, which significantly expands the AR bandwidth of the antenna and effectively enhances the CP radiation performance.

To determine the excitable modes, the modal weighting coefficients (MWCs) were observed. As shown in Fig. 2(d), the MWC simulation results for the proposed metamaterial surface antenna indicate that Modes 2, 4, 5, and 9 can be excited within the frequency range of 5 GHz to 8 GHz. Specifically, Modes 2 and 4 can be excited together below 6.5 GHz, while Modes 5 and 9 can be excited together above 6.5 GHz.

The characteristic currents of the target modes (Modes 2, 4, 5, and 9) show significant field strength distribution in the central region of the metasurface. To synchronously excite these two groups of orthogonal modes for broadband CP radiation, the rectangular coupling slot is placed directly below the metasurface central region, whose spatial position is aligned with the current field strength extreme points of each mode. Multi-mode cooperative operation is directly excited through spatial

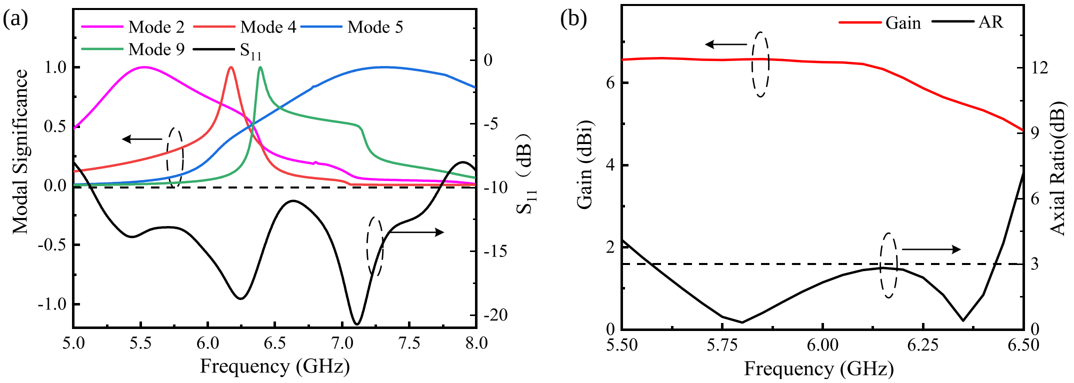

FIGURE 3. (a) MS and S_{11} performance. (b) AR and realized gain performance.

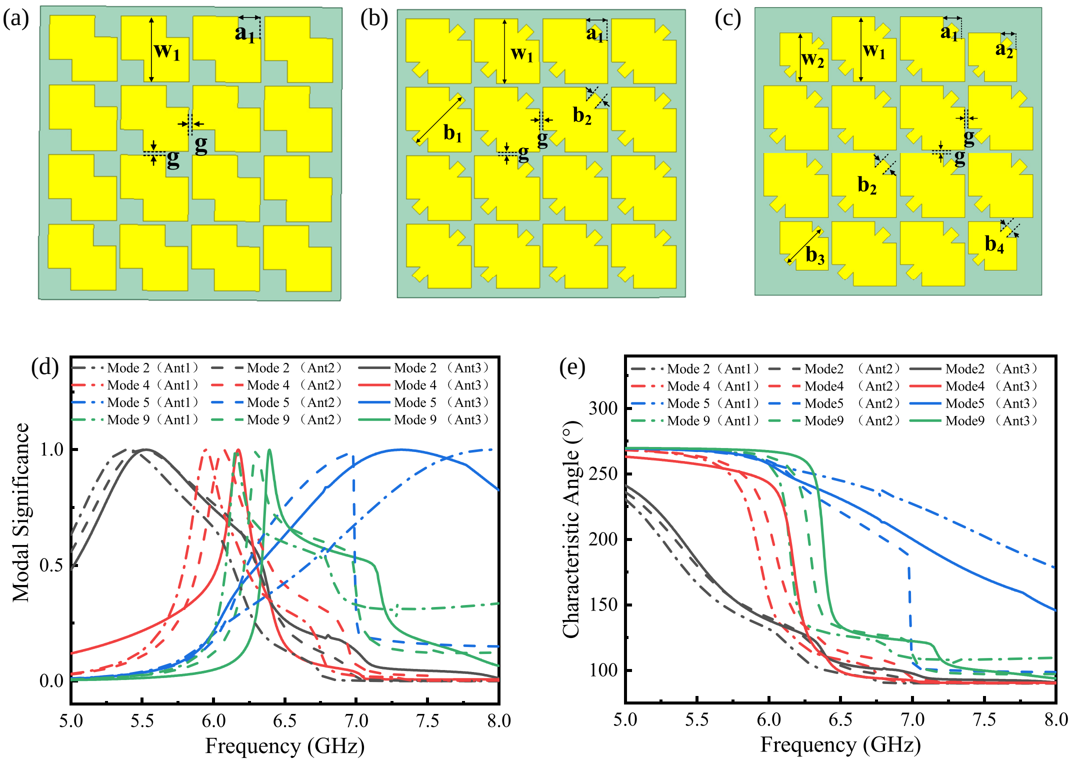

FIGURE 4. (a) Antenna 1. (b) Antenna 2. (c) Antenna 3. (d) Comparative MS plots for Ant. 1–Ant. 3. (e) Comparative CA plots for Ant. 1–Ant. 3.

electromagnetic coupling, thereby satisfying the amplitude and phase constraint conditions for CP generation.

After adding the feeding structure, the metasurface antenna was simulated, and the S_{11} parameter and AR are shown in Fig. 3. It can be observed that the -10 dB impedance bandwidth of the antenna is 40.37% (5.14–7.74 GHz), and there are three resonance points within the impedance bandwidth. Among them, the resonance point at 5.43 GHz corresponds to the mode significance (MS) value of 1 for Mode 2 as shown in Fig. 2(a); the resonance point at 6.25 GHz corresponds to the MS value of 1 for both Mode 4 and Mode 5, and the resonance points of Mode 4 and Mode 5 are close to each other, thus merging into a single resonance point; the resonance point at 7.11 GHz corresponds to the MS value of 1 for Mode 9. The correspondence between the S_{11} values and the characteristic mode resonance points further verifies the correctness of the characteristic mode analysis. The 3 dB AR bandwidth of the antenna is 14.33% (5.57–6.43 GHz), which also has two resonance points within the AR bandwidth. The frequencies at 5.8 GHz and 6.35 GHz also correspond to the frequencies when the characteristic angle difference is 90°. Moreover, the maximum gain within the effective AR bandwidth reaches 6.6 dBi.

2.3. Antenna Design Process

To illustrate the design path of the CP metasurface antenna element, Fig. 5 presents a more intuitive evolutionary process of the antenna structure from Ant. 1 to Ant. 3. The design flow is described as follows:

Step 1: As shown in Fig. 4(a), Ant. 1 is adopted as the initial configuration, which employs a 4×4 metasurface structure realized by cutting rectangular regions with a size of $a1$ at the

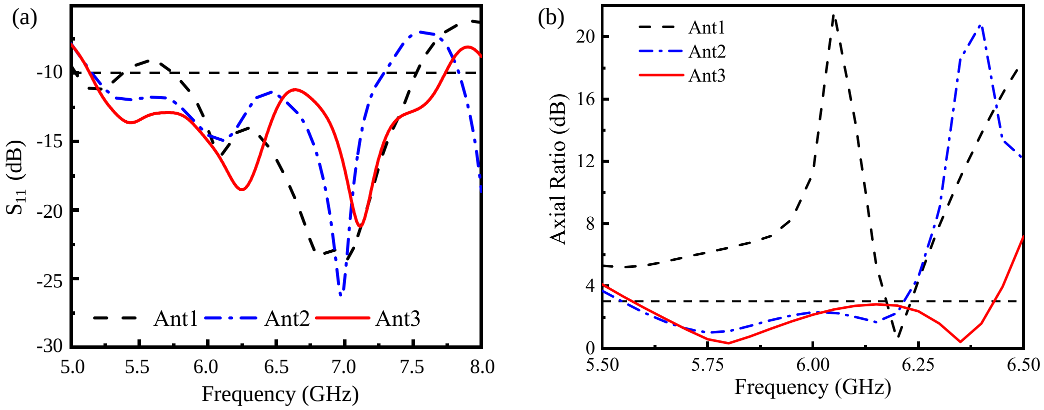

FIGURE 5. (a) Comparative S_{11} performance for Ant. 1–Ant. 3. (b) Comparative AR performance for Ant. 1–Ant. 3.

upper right and lower left corners. As illustrated in Figs. 4(d) and (e), Mode 5 and Mode 9 are effectively excited, dominating at 6 GHz and 7 GHz, respectively, and the phase difference reaches 90° at 6.25 GHz, resulting in narrow-bandwidth CP radiation. Figs. 5(a) and (b) also confirm that the S_{11} parameter is greater than -10 dB at 5.5 GHz, and Mode 2 and Mode 4 are not effectively excited. Consequently, although a 90° phase difference is also formed, no AR resonance point is generated. Finally, the simulated -10 dB impedance bandwidth of Ant. 1 is 5.74–7.52 GHz (26.85%), and the 3 dB AR bandwidth is 6.16–6.24 GHz (1.29%).

Step 2: To enhance the excitation efficiency of Mode 2 and Mode 4 in the low-frequency band, a rectangular patch with a length of $b1$, a width of $b2$, and rotated by 45° is added in the center of each metasurface unit, forming Ant. 2 as shown in Fig. 4(b). As presented in Figs. 4(d) and (e), the overall frequency bands of Mode 2 and Mode 4 shift to the high-frequency region and can be effectively excited, while Mode 5 and Mode 9 shift to the low-frequency region. However, the sharp drop in the MS value of Mode 5 at 7 GHz adversely affects the impedance bandwidth in the high-frequency band, and the 90° phase difference formed by the CA of Mode 5 and Mode 9 also shifts to the low-frequency region, leading to a low-frequency shift of the AR resonance point in the high-frequency band. Figs. 5(a) and (b) also verify that Mode 2 is effectively excited, forming a resonance point for impedance bandwidth at 5.5 GHz. In addition, two AR resonance points are formed by the two sets of orthogonal modes at 5.75 GHz and 6.13 GHz. Finally, the simulated impedance bandwidth of Ant. 2 is 5.15–7.29 GHz (34.41%), and the 3 dB AR bandwidth is 5.55–6.22 GHz (11.39%).

Step 3: To further optimize the excitation effect of the four modes and continuously expand the operating bandwidth, the final design evolves to Ant. 3, as shown in Fig. 4(c). In this configuration, the sub-patches at the four corners of the metasurface patch are scaled down to 0.75 times the original size, while the size of the central patch remains unchanged. Compared with Ant. 2, as shown in Figs. 4(d) and (e), Ant. 3 shifts the response frequencies of Mode 5 and Mode 9 to the high-frequency region and successfully eliminates the sharp drop in the MS value of Mode 5 at 7 GHz. Meanwhile, the 90° phase difference generated by the CA also shifts to the high-frequency region, effectively expanding the AR bandwidth. Figs. 5(a) and (b) also confirm that the impedance bandwidth of Ant. 3 is effectively expanded, and the AR bandwidth is also effectively extended in the high-frequency region. Finally, the simulated -10 dB impedance bandwidth of Ant. 3 is 5.14–7.74 GHz (40.37%), and the 3 dB AR bandwidth is 5.57–6.43 GHz (14.33%). This fully demonstrates the significant effect of continuously evolving the antenna structure through characteristic mode analysis on improving the overall performance of the antenna.

2.4. Surface Current Distributions

To more intuitively understand the CP working mechanism of the antenna, simulations of the current distribution of the metasurface radiation layer at different phase moments were carried out, and the following conclusions were drawn. As shown in Fig. 6, at a frequency of 5.8 GHz, the current polarization directions of the metasurface radiation layer at the phases of 0° and 90° are $-45°$ and 45°, respectively, which are mutually perpendicular. At a frequency of 6.35 GHz, the current polarization directions of the metasurface radiation layer at the phases of 0° and 90° are also $-135°$ and $-45°$, respectively, and are mutually perpendicular. This fully demonstrates that the metasurface antenna effectively achieves right-hand circular polarization (RHCP) radiation.

2.5. Four-Port MIMO Antenna Design

Figure 7 shows the structure of the proposed four-port MIMO antenna, with an overall size of $80 \times 80 \times 2.6\,\text{mm}^3$. It is formed by modifying and rotating the CP antenna element proposed in Fig. 1. Specifically, the size of the patches at the four corners of each monopole CP metasurface unit is adjusted to 0.8 times its original scale, and the monopole antennas are rotated counterclockwise by 90° in sequence to form a 2×2 MIMO antenna. When the four ports are excited separately, the antenna radiates left-hand circularly polarized (LHCP) waves.

To clearly illustrate the performance of the four-port antenna, Fig. 8 presents the simulated results of its S-parameters and AR values. As shown in Fig. 8(a), the impedance bandwidth is 5.10–7.65 GHz (40%). The 3 dB AR bandwidth, depicted in Fig. 8(b), is 5.34–6.39 GHz (17.9%). Within this effective axial

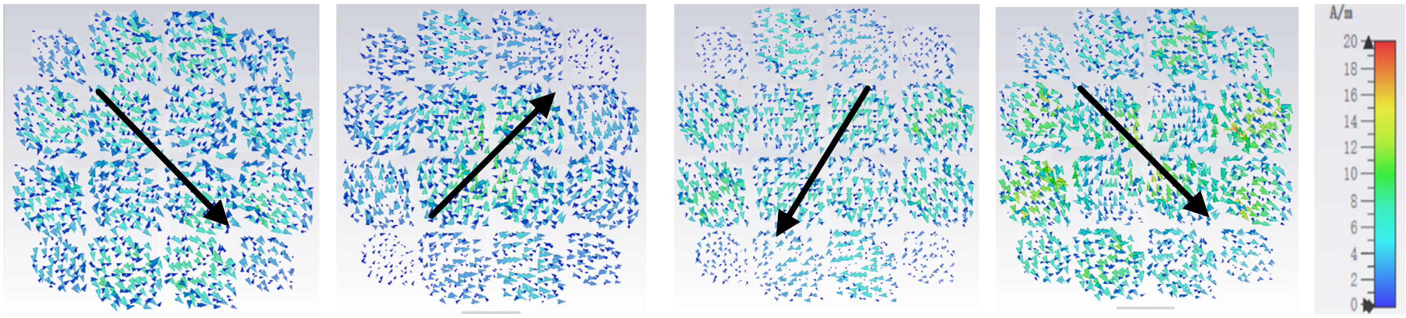

5.8GHz , 0°   5.8GHz , 90°   6.35GHz , 0°   6.35GHz , 90°

FIGURE 6. Surface current distributions on the metasurface radiating layer at different phase instants.

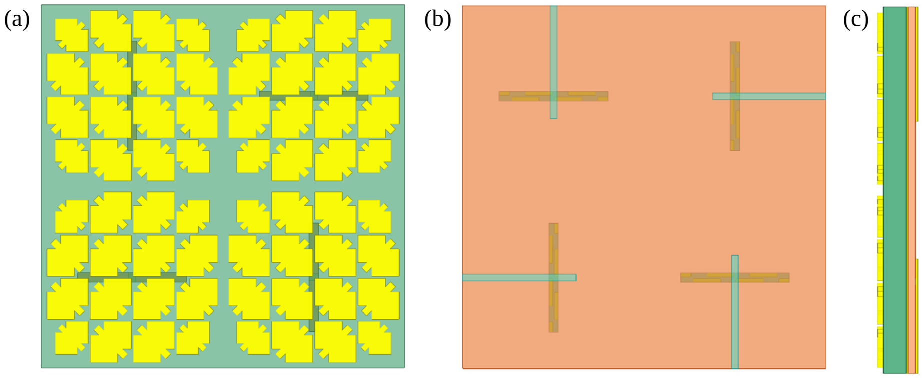

FIGURE 7. (a) Front view of MIMO antenna. (b) Rear view of MIMO antenna. (c) Side view of MIMO antenna.

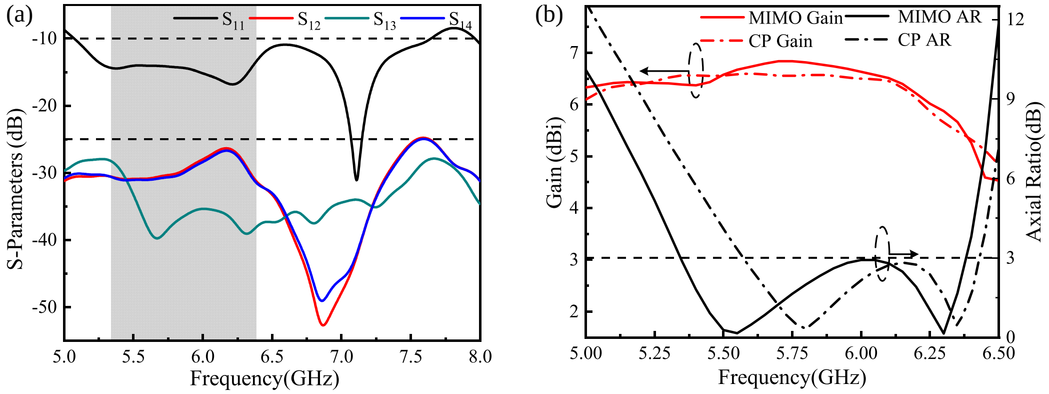

FIGURE 8. (a) S-parameters of the MIMO antenna. (b) AR and gain performance of the MIMO antenna.

ratio bandwidth, the antenna can achieve a maximum gain of up to 6.84 dBi. Compared with the aforementioned monopole CP antenna element, the 2×2 MIMO antenna exhibits significant improvements in both AR bandwidth and maximum gain.

The mutual coupling between MIMO elements can be characterized by the transmission coefficients. The simulated transmission coefficients are shown in Fig. 9(a). The antenna exhibits high isolation performance without the need for additional decoupling structures. Within the AR bandwidth, the minimum isolation between antenna elements is better than -25 dB. This advantage is attributed to the metasurface elements between the antenna units, which act as a decoupling structure. The mechanism for reducing mutual coupling between MIMO elements is achieved by introducing periodic structures between adjacent antenna units. Among the transmission coefficients, S_{13} has a lower value because these two antennas are located at diagonal positions, with a longer spacing compared to other adjacent antennas.

For the MIMO antenna system, the envelope correlation coefficient (ECC) between array elements can be calculated based on the S-parameters through Equation (1) [20]. Within the operating frequency band, the envelope correlation coefficient calculated by Equation (1) is extremely low, only 0.0002, as shown in Fig. 9(a). This indicates that the proposed MIMO an-

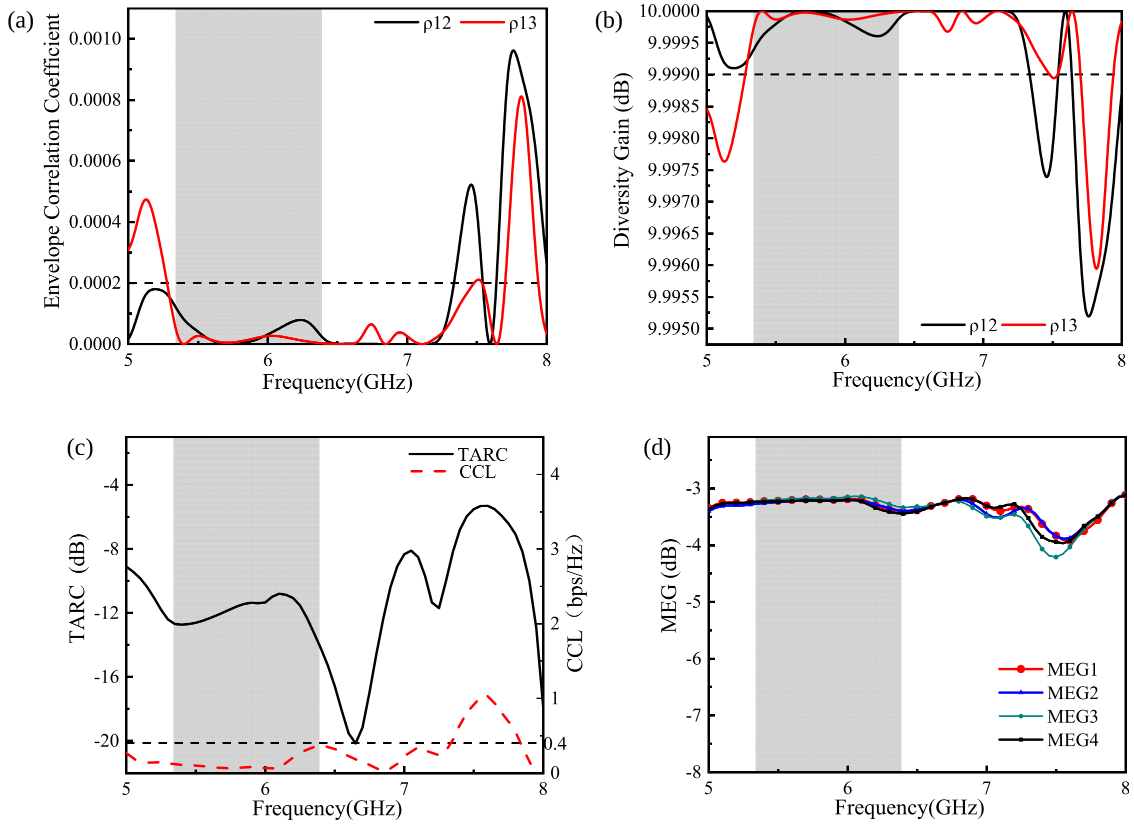

FIGURE 9. (a) ECC of the MIMO antenna. (b) DG of the MIMO antenna. (c) TARC and CCL of the MIMO antenna. (d) MEG of the MIMO antenna.

tenna possesses excellent diversity performance.

$$\rho_{ij} = \frac{\left|\iint_{4\pi}^{\pi} F_i(\theta,\phi)\cdot F_j^*(\theta,\phi)\,d\Omega\right|^2}{\iint_{4\pi}^{\pi} |F_i(\theta,\phi)|^2 d\Omega \cdot \iint_{4\pi}^{\pi} |F_j(\theta,\phi)|^2 d\Omega} \tag{1}$$

Diversity gain (DG) is another fundamental parameter describing the impact of the diversity scheme on radiated power. The DG of the proposed MIMO antenna is calculated as a function of frequency using the relationship in Equation (2), as shown in Fig. 9(b). The diversity gain of the antenna elements is above 9.9990 dB, which is very close to the ideal value of 10 dB.

$$\mathrm{DG} = 10\sqrt{1-|\rho_{eij}|^2} \tag{2}$$

For MIMO antenna systems, since S-parameters cannot fully predict actual scenarios, it is necessary to calculate the total effective reflection coefficient (TARC) of the antenna. TARC can be calculated based on S-parameters using the following formula:

$$\mathrm{TARC} = \frac{\sqrt{\sum_{i=1}^{N}\left|S_{i1}+\sum_{n=2}^{N} S_{in}e^{j\theta_{n-1}}\right|^2}}{\sqrt{N}} \tag{3}$$

Channel capacity loss (CCL) is also an important parameter in MIMO antennas. Generally, a CCL value below 0.4 bps/Hz is sufficient to meet the design requirements of MIMO antennas. The expression for CCL is

$$\mathrm{CCL} \;=\; -\log_2 \det\left|\psi^R\right| \tag{4}$$

$$\psi^R = \begin{pmatrix} \rho_{11} & \cdots & \rho_{1n} \\ \vdots & \ddots & \vdots \\ \rho_{m1} & \cdots & \rho_{mn} \end{pmatrix} \tag{5}$$

The calculation results shown in Fig. 9(c) indicate that for MIMO antennas, within the 3 dB axial ratio bandwidth, the transmission reflection gain (TRAC) is less than -10 dB, and the coupling loss (CCL) is below 0.4 bps/Hz. This further demonstrates that the antenna exhibits extremely low coupling, ensuring channel independence and non-interference during signal reception and transmission, thereby enhancing system capacity.

To evaluate the diversity performance of the multi-input multi-output (MIMO) system, the multi-input gain (MEG) is defined as the ratio of the average power received by the MIMO antenna to the power received by the omnidirectional antenna. For an N-port antenna system, MEG can be calculated according to formula (6).

$$\mathrm{MEG}_i = 0.5\left(1-\sum_{j=1}^{N}|S_{ij}|^2\right) \tag{6}$$

Here, N represents the number of antennas, and i and j represent the antenna port numbers. The MEG value required to exhibit good diversity characteristics should be $-12\,\mathrm{dB} < \mathrm{MEG} < -3\,\mathrm{dB}$. Fig. 9 shows that the simulated MEG of the proposed four-port MIMO antenna is within a reasonable range and has excellent diversity performance.

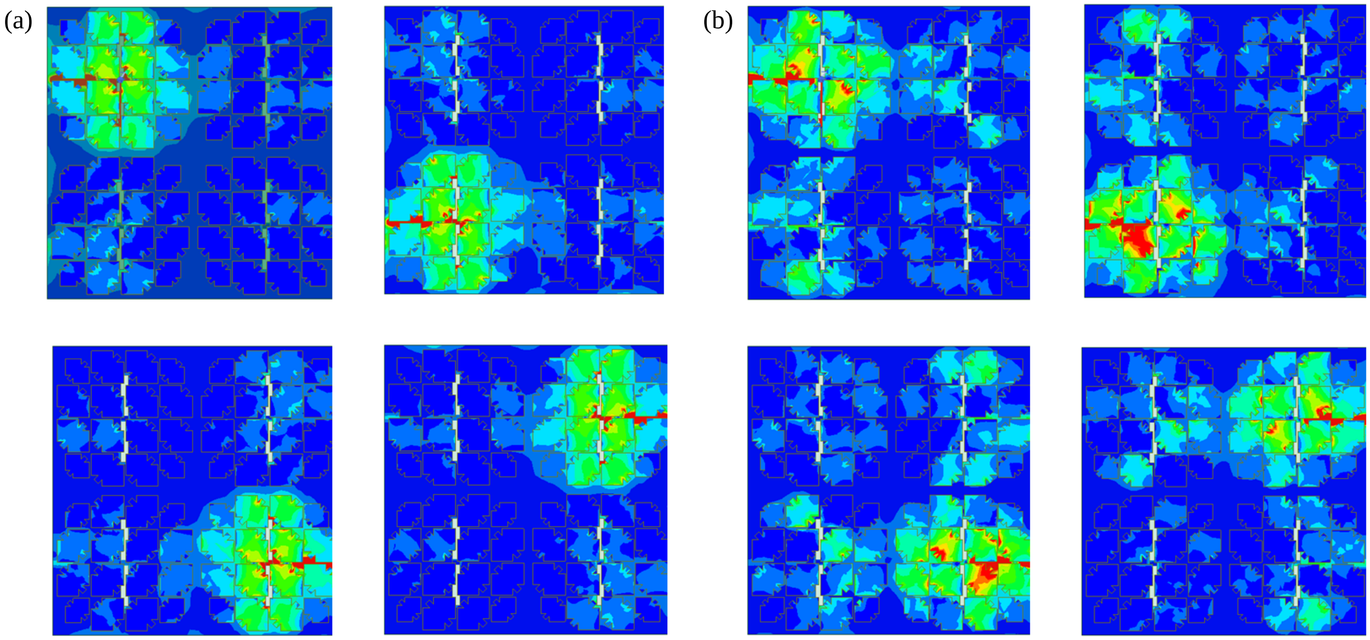

FIGURE 10. The surface current distribution of the antenna. (a) 5.55 GHz, (b) 6.3 GHz.

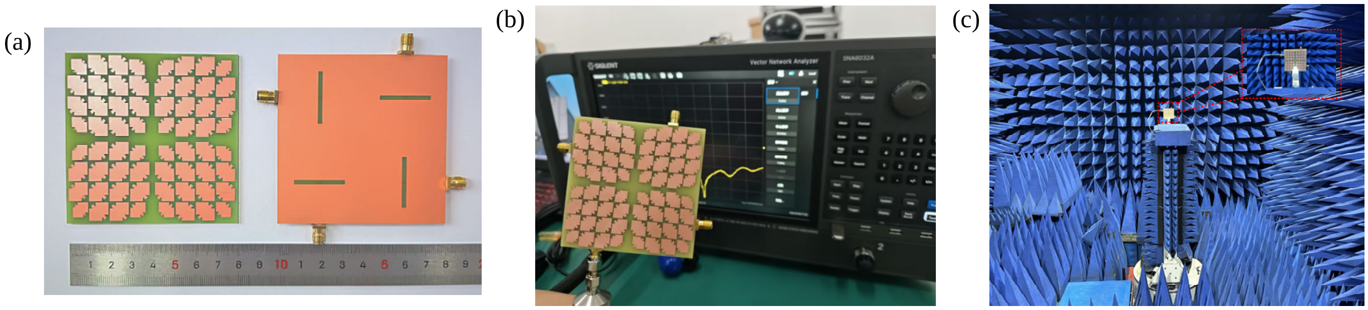

FIGURE 11. Photograph of the prototype in the measurement.

As shown in Fig. 10, when each port is excited at 5.55 GHz and 6.3 GHz, respectively, the surface current density of the MIMO antenna presents highly localized distribution characteristics: the current is mainly concentrated on the metasurface unit corresponding to the excited port, and the current density in the unexcited port units (especially the diagonal units) is close to 0 (less than 1 A/m). This distribution characteristic is due to the gradient-scaled metasurface structure forming an electromagnetic barrier between the array units, which truncates the propagation path of surface waves and suppresses the space wave coupling between units. For the adjacent ports (e.g., Port 1 and Port 2), a small amount of weak coupled current is observed at the edge of the metasurface units, but the current intensity is less than 4 A/m, which is far lower than the current intensity of the excited port (15–20 A/m), thus ensuring high port isolation ($>$ 25 dB). For the diagonal ports (e.g., Port 1 and Port 3), almost no coupled current is observed, which is consistent with the lower transmission coefficient (S_{13}) in the S-parameter test results, further verifying the excellent self-decoupling capability of the proposed metasurface geometry.

3. RESULTS AND DISCUSSION

3.1. Measurement and Simulation

S-parameters were measured using a vector network analyzer (VNA), while radiation patterns and gain were characterized with a standard gain horn antenna in an anechoic chamber (test setup: Figs. 11(a)–(c)). Figs. 12(a) and (b) present the comparison between the measured and simulated results of the antenna array, and the results are highly consistent with minor deviations, which are mainly attributed to fabrication tolerances of the antenna structure and welding errors of the SMA connector. It is worth noting that the resonance points remain relatively stable despite the slight S-parameter deviations caused by the above factors, verifying the good manufacturability of the proposed antenna. The measured -10 dB impedance bandwidth is 5.07–7.76 GHz (41.93%), and the 3 dB AR bandwidth is 5.37–6.40 GHz (17.5%), while the simulated coverage ranges are 5.10–7.65 GHz (40%) and 5.34–6.39 GHz (17.9%), respectively. Within the 3 dB AR bandwidth, the measured gain achieves 6.77 dBi, and the maximum simulated gain is 6.84 dBi, with a small deviation between the two.

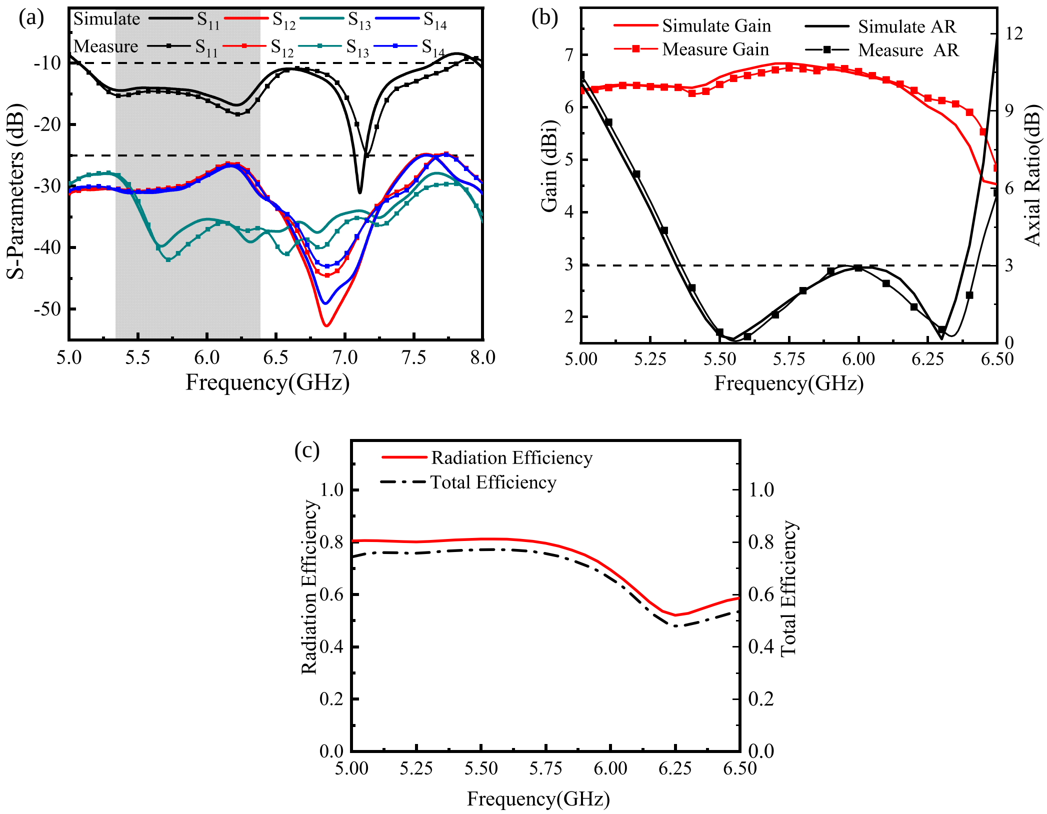

FIGURE 12. Simulated versus measured results. (a) Reflection coefficient of the proposed antenna. (b) Gain and AR performance of the proposed antenna. (c) Radiation efficiency and total efficiency.

TABLE 1. Antenna performance comparison.

Ref.	-10 dB BW(%)	3 dB ARBW(%)	Isolation (dB)	Gain (dBi)	Size (λ_0^3)	Printed layers	Array
[21]	9	10.9	NA	3	$0.17 \times 0.58 \times 0.006$	1	1×1
[22]	16	11.2	NA	4.7	$0.98 \times 0.98 \times 0.03$	1	1×1
[23]	30.15	14	> 55	18.5	$4.6 \times 4.6 \times 0.128$	1	2×2
[24]	11.13	3.69	> 23	4.77	$1.55 \times 2.92 \times 1.55$	2	2×2
[25]	36.0	22.4	> 15	11.22	$1.40 \times 1.40 \times 0.069$	2	2×2
[26]	40.96	27.42	NA	11.15	$1.46 \times 1.46 \times 0.076$	2	2×2
This work	41.93	17.5	> 25	6.77	$1.60 \times 1.60 \times 0.052$	2	2×2

λ_0 is the free-space wavelength at center operating frequency

As shown in Fig. 12(c), within the effective AR bandwidth range, the measured radiation efficiency of this antenna varies between 55% and 80%, while the total efficiency ranges from 50% to 77%. Due to the high loss of FR4 material at high frequencies, the radiation efficiency and total efficiency decrease at high frequencies, but the overall trend remains relatively gentle. For the high-frequency band above 7 GHz, the S-parameter deviation is slightly larger than that in the low-frequency band but still falls within an acceptable range; meanwhile, the gain decreases moderately due to the dielectric loss of the FR4 substrate at high frequencies but remains above 4.5 dBi, which fully demonstrates the excellent robustness of the antenna in the entire operating bandwidth. In addition, the FR4 substrate adopted in this design is a commercial low-cost dielectric material (only one-fifth the cost of Rogers series high-frequency substrates), and the simple three-metal-layer single-feed structure of the antenna is compatible with standard printed circuit board (PCB) manufacturing processes, enabling low-cost mass production and having prominent engineering application value.

Figure 13 shows the measured and simulated radiation patterns at 5.55 GHz and 6.3 GHz. This antenna generates stable, symmetrical, and unidirectional side-edge radiation patterns through LHCP radiation. The measured results are highly consistent with the simulated results. At both frequencies, LHCP radiation always dominates, while RHCP radiation is in a secondary position. The measured cross-polarization level (RHCP) within the main beam is always lower than -15 dB,

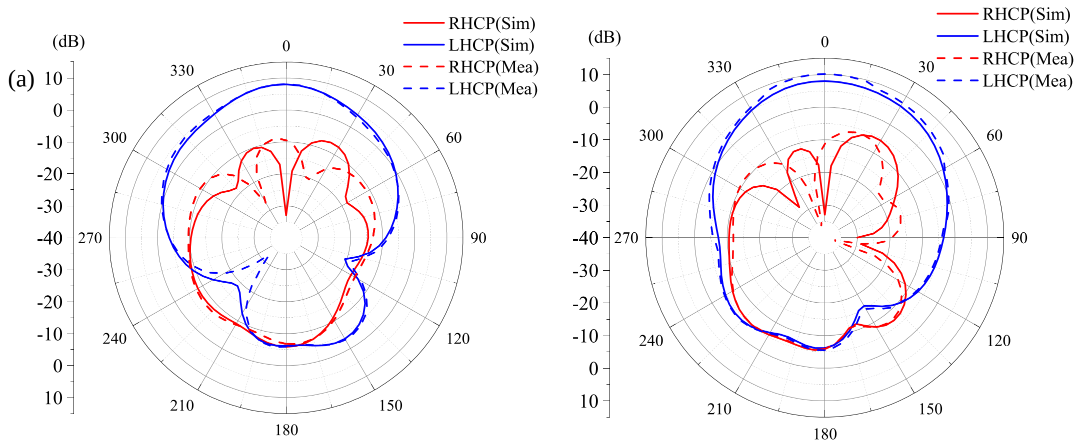

xoz-plane at 5.55GHz

yoz-plane at 5.55GHz

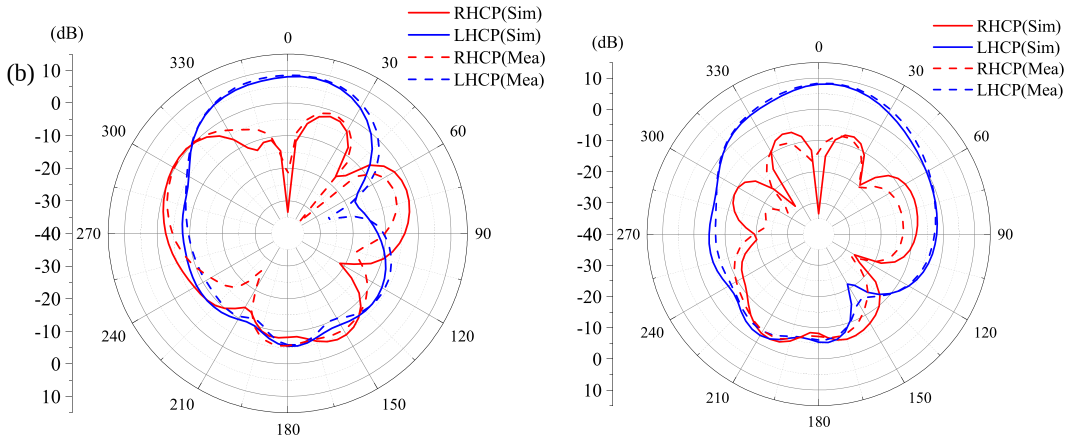

xoz-plane at 6.3GHz

yoz-plane at 6.3GHz

FIGURE 13. Numerically simulated and experimentally measured radiation patterns of the developed antenna at (a) 5.55 GHz, (b) 6.3 GHz.

and the cross-polarization discrimination exceeds 10 dB, confirming extremely high polarization purity. Furthermore, this is further confirmed by the symmetrical and clear zero points in the RHCP radiation pattern matching the peak of the LHCP main beam.

3.2. Antenna Performance Comparison

Table 1 further quantifies the performance advantages of the proposed antenna over the existing CP MIMO antennas based on CMA and broadband CP antenna arrays. Compared with the CP antennas that combine two linear polarization modes, the four-mode cooperative excitation strategy adopted in this paper effectively extends the 3 dB AR bandwidth to 17.5%, which is significantly higher than those of the CP antennas reported in [21] (10.9%), [22] (11.2%), and [23] (14%). For the CP antennas with additional decoupling and feeding structures, the proposed metasurface self-decoupling mechanism achieves a port isolation greater than 25 dB, outperforming those in [24] (greater than 23 dB) and [25] (greater than 15 dB). In addition, unlike the antenna in [26], it does not employ a complex feeding network, demonstrating obvious structural advantages. The proposed antenna achieves a more balanced trade-off among impedance bandwidth, AR bandwidth, port isolation, and structural simplicity, featuring high integration and a scalable design that meets the requirements of practical MIMO communication systems.

4. CONCLUSION

In this paper, a four-mode CP metasurface 2×2 MIMO antenna based on CMA is proposed and implemented. The mechanisms of characteristic mode excitation, circular polarization realization, feeding matching, and array mutual coupling suppression are systematically studied. Guided by CMA, the antenna structure is designed: corner truncation is performed on the radiating patch, and a central rotated stub is introduced to effectively generate the phase difference required for circular polarization. A microstrip-slot coupled feeding method is adopted to accurately match the extreme points of modal currents, synchronously exciting two sets of orthogonal characteristic modes to achieve broadband CP radiation. The designed 2×2 MIMO array achieves mutual coupling suppression by virtue of the metasurface structure itself, with a port isolation better than 25 dB without any additional decoupling structures. Measurement results show that the antenna has a relative impedance bandwidth of 41.93% (5.07–7.76 GHz), an AR relative bandwidth of 17.5% (5.37–6.40 GHz), a peak gain of 6.77 dBi, an array ECC as low as 0.0002, and a DG close to 10 dB. Compared with existing similar works, the proposed antenna achieves a better balance in terms of broadband impedance characteristics, excellent circular polarization performance, ultra-high port isolation, and structural simplicity, with the advantages of high integration, low profile, and easy conformal design. This work verifies the effectiveness of CMA in the collaborative design of metasurface MIMO antennas and can provide reference ideas and technical support for the design of high-performance CP MIMO antennas in the Sub-6 GHz, UAV communication, and wireless local area network frequency bands.

ACKNOWLEDGEMENT

This work was supported in part by the Natural Science Research Project of Anhui Educational Committee under Grant No. 2025AHGXZK31006, in part by the Research Foundation of Jiangsu Engineering Research Center for Bionics Control Technology and Equipment under Grant No. FSKZ202503, in part by the Anhui International Joint Research Center for Ancient Architecture Intellisencing and Multi-Dimensional Modeling under Grant No. GJZZX2025KF03.

REFERENCES

[1] Wu, D., Y.-X. Sun, R. Lian, B. Xiao, M. Li, and K.-D. Xu, "Metasurface antenna with cocircularly polarized radiation characteristics for wideband monostatic simultaneous transmit and receive applications," *IEEE Transactions on Antennas and Propagation*, Vol. 71, No. 4, 3304–3313, Apr. 2023.

[2] Xu, R., J. Liu, K. Wei, W. Hu, Z.-J. Xing, J.-Y. Li, and S. S. Gao, "Dual-band circularly polarized antenna with two pairs of crossed-dipoles for RFID reader," *IEEE Transactions on Antennas and Propagation*, Vol. 69, No. 12, 8194–8203, Dec. 2021.

[3] Liu, S., Z. Wang, and Y. Dong, "Compact wideband SRR-inspired antennas for 5G microcell applications," *IEEE Transactions on Antennas and Propagation*, Vol. 69, No. 9, 5998–6003, Sep. 2021.

[4] Li, P., Y. Zhang, X. Qin, K. Wei, P. Liang, and Y. Li, "Wideband widebeam circular-polarized antenna using asymmetrical tri-dipoles for direct satellite-to-handset communications," *IEEE Transactions on Antennas and Propagation*, Vol. 72, No. 8, 6270–6277, Aug. 2024.

[5] El Yousfi, A., A. Lamkaddem, K. A. Abdalmalak, and D. Segovia-Vargas, "A broadband circularly polarized single-layer metasurface antenna using characteristic-mode analysis," *IEEE Transactions on Antennas and Propagation*, Vol. 71, No. 4, 3114–3122, Apr. 2023.

[6] Gao, X., G. Tian, Z. Shou, and S. Li, "A low-profile broadband circularly polarized patch antenna based on characteristic mode analysis," *IEEE Antennas and Wireless Propagation Letters*, Vol. 20, No. 2, 214–218, Feb. 2021.

[7] Amn-E-Elahi, A., P. Rezaei, F. Karami, F. Hyjazie, and H. Boutayeb, "Analysis and design of a stacked PCBs-based quasi-helix antenna," *IEEE Transactions on Antennas and Propagation*, Vol. 70, No. 12, 12 253–12 257, Dec. 2022.

[8] Lin, J.-F. and L. Zhu, "Low-profile high-directivity circularly-polarized differential-fed patch antenna with characteristic modes analysis," *IEEE Transactions on Antennas and Propagation*, Vol. 69, No. 2, 723–733, Feb. 2021.

[9] Li, W., S. Gao, Y. Cai, Q. Luo, M. Sobhy, G. Wei, J. Xu, J. Li, C. Wu, and Z. Cheng, "Polarization-reconfigurable circularly polarized planar antenna using switchable polarizer," *IEEE Transactions on Antennas and Propagation*, Vol. 65, No. 9, 4470–4477, Sep. 2017.

[10] Garbacz, R. J., "Modal expansions for resonance scattering phenomena," *Proceedings of the IEEE*, Vol. 53, No. 8, 856–864, Aug. 1965.

[11] Liu, N.-W., L. Zhu, Z.-X. Liu, M. Li, G. Fu, and Y. Liu, "A novel low-profile circularly polarized diversity patch antenna with extremely small spacing, reduced size, and low mutual coupling," *IEEE Transactions on Antennas and Propagation*, Vol. 70, No. 1, 135–144, Jan. 2022.

[12] Juan, Y., W. Yang, and W. Che, "Miniaturized low-profile circularly polarized metasurface antenna using capacitive loading," *IEEE Transactions on Antennas and Propagation*, Vol. 67, No. 5, 3527–3532, May 2019.

[13] Zeng, J., X. Liang, L. He, F. Guan, F. H. Lin, and J. Zi, "Single-fed triple-mode wideband circularly polarized microstrip antennas using characteristic mode analysis," *IEEE Transactions on Antennas and Propagation*, Vol. 70, No. 2, 846–855, Feb. 2022.

[14] Xu, R., S. S. Gao, J. Liu, J.-Y. Li, Q. Luo, W. Hu, L. Wen, X.-X. Yang, and J. T. S. Sumantyo, "Analysis and design of ultrawideband circularly polarized antenna and array," *IEEE Transactions on Antennas and Propagation*, Vol. 68, No. 12, 7842–7853, Dec. 2020.

[15] Kulkarni, J., C.-Y.-D. Sim, B. Garner, and Y. Li, "A dual-CP quad-port MIMO antenna with reduced mutual coupling for X-band application," *IEEE Antennas and Wireless Propagation Letters*, Vol. 22, No. 9, 2085–2089, Sep. 2023.

[16] Chattha, H. T., F. Latif, F. A. Tahir, M. U. Khan, and X. Yang, "Small-sized UWB MIMO antenna with band rejection capability," *IEEE Access*, Vol. 7, 121 816–121 824, 2019.

[17] Yang, W. J., Y. M. Pan, and S. Y. Zheng, "Mutual coupling reduction in CP MIMO crossed-dipole antenna array," *IEEE Antennas and Wireless Propagation Letters*, Vol. 21, No. 12, 2442–2446, Dec. 2022.

[18] Wu, R., J.-H. Lin, J.-F. Li, and F.-C. Chen, "Wideband circularly polarized antenna with novel asymmetric Y-shaped arms," *IEEE Antennas and Wireless Propagation Letters*, Vol. 23, No. 4, 1181–1185, Apr. 2024.

[19] Zeng, J., Z. Zhang, F. H. Lin, and F. Guan, "Penta-mode ultrawideband circularly polarized stacked patch antennas using characteristic mode analysis," *IEEE Transactions on Antennas and Propagation*, Vol. 70, No. 10, 9051–9060, Oct. 2022.

[20] Feng, H., Z. Wang, W. Nie, and M. Yang, "High-gain dual-band metasurface MIMO antenna for enhanced 5G and satellite applications," *Progress In Electromagnetics Research C*, Vol. 156, 13–22, 2025.

[21] Wang, Z., Y. Liu, and Y. Dong, "Novel miniaturized circularly polarized inverted-F antenna with planar configuration," *IEEE Antennas and Wireless Propagation Letters*, Vol. 23, No. 3, 1005–1009, Mar. 2024.

[22] Kumar, K., S. Dwari, and M. K. Mandal, "Broadband dual circularly polarized substrate integrated waveguide antenna," *IEEE Antennas and Wireless Propagation Letters*, Vol. 16, 2971–2974, 2017.

[23] Kanakavalli, H., R. Pandeeswari, and S. Gupta, "Metasurface-inspired circularly polarized MIMO antenna for 5G mmWave applications," *IEEE Antennas and Wireless Propagation Letters*, Vol. 24, No. 2, 434–438, Feb. 2025.

[24] Sofi, M. A., K. Saurav, and S. K. Koul, "Four-port orthogonal circularly polarized dual-band MIMO antenna with polarization

and spatial diversity using a dual-band linear-to-circular polarization converter," *IEEE Transactions on Antennas and Propagation*, Vol. 70, No. 9, 8554–8559, Sep. 2022.

[25] Yang, W., Q. Meng, W. Che, L. Gu, and Q. Xue, "Low-profile wideband dual-circularly polarized metasurface antenna array with large beamwidth," *IEEE Antennas and Wireless Propagation Letters*, Vol. 17, No. 9, 1613–1616, Sep. 2018.

[26] Ye, J., T. Li, M. Han, and W. Dou, "Metasurface-inspired wideband circularly polarized antenna array in Ka-band using characteristic mode analysis," *IEEE Antennas and Wireless Propagation Letters*, Vol. 23, No. 1, 389–393, Jan. 2024.